



Modeling solar flare induced lower ionosphere changes using VLF/LF transmitter amplitude and phase observations at a midlatitude site

E. D. Schmitter

University of Applied Sciences Osnabrück, 49076 Osnabrück, Germany

Correspondence to: E. D. Schmitter (e.d.schmitter@hs-osnabrueck.de)

Received: 18 November 2012 – Revised: 28 February 2013 – Accepted: 9 April 2013 – Published: 26 April 2013

Abstract. Remote sensing of the ionosphere bottom using long wave radio signal propagation is a still going strong and inexpensive method for continuous monitoring purposes. We present a propagation model describing the time development of solar flare effects. Based on monitored amplitude and phase data from VLF/LF transmitters gained at a mid-latitude site during the currently increasing solar cycle no. 24 a parameterized electron density profile is calculated as a function of time and fed into propagation calculations using the LWPC (Long Wave Propagation Capability). The model allows to include lower ionosphere recombination and attachment coefficients, as well as to identify the relevant forcing X-ray wavelength band, and is intended to be a small step forward to a better understanding of the solar–lower ionosphere interaction mechanisms within a consistent framework.

Keywords. Ionosphere (Ionospheric disturbances)

1 Introduction

Remote sensing of lower ionosphere conditions by monitoring low and very low frequency radio signal propagation is a well-known method for several decades. MSK (minimum shift keying) transmitters prove as useful in this respect because of their constant amplitude emissions. We have analyzed the signal amplitude and phase variations of 2 transmitters, NRK/TFK (37.5 kHz, 63.9° N, 22.5° W, Iceland) and GBZ (19.58 kHz, 54.9° N, 3.3° W, UK) received at a midlatitude site (52° N, 8° E) with great-circle distances of 2210 and 800 km, respectively. The time stability of both transmitters proved to be sufficient for continuous day and night over monitoring not only of the amplitude but also of the phase.

The NW paths as seen from our midlatitude site are particularly suited to study lower ionosphere forcing from above with regard to auroral and sub-auroral particle precipitation (Schmitter, 2010) as well as forcing from below by planetary wave activity (Schmitter, 2012). The model presented is able to map the complete day-night variation of the lower ionosphere during quiet and disturbed conditions. In this paper we focus on the direct effects of solar flare X-rays.

Solar flares are powered by the sudden release of magnetic field energy in active regions accelerating electrons and ions to relativistic velocities. The same energy release may also cause coronal mass ejections (CMEs) to space. The flare spectrum in the soft X-ray photon energy range 1–20 keV which is of importance for the forcing of the lower ionosphere is dominated by bremsstrahlung of electrons in a hot thermal plasma above the solar photosphere. “Hot” means electron temperatures T_e typically in the range of 10–25 megaKelvin or more. The spectral flux (photons $\text{keV}^{-1} \text{m}^{-2}$) decreases quasi-exponentially with photon energy E as $1/(E T_e^{0.5}) \cdot e^{-E/(k T_e)}$. Line radiation (mainly 6.7 keV (Fe) and 8.0 keV (Fe/Ni)) is superimposed to the bremsstrahlung continuum, its intensity increasing with T_e (Doshchek, 1999; Phillips, 2004; Aschwanden, 2008).

We base our model on the framework of the Wait and Spies two-parameter e-density profile for the lower ionosphere (60–85 km height, Wait and Spies, 1964) being aware that this is an oversimplification of the true density profile (cp. Aiken, 1969, Fig. 1 therein, for e-density profiles from rocket firings during quiet and flare conditions and see Fig. 5 in this paper with our two-parameter β , h' approximations to model profiles from Nicolet and Aikin, 1960). However, only the bottom part of the ionosphere is really sensed by

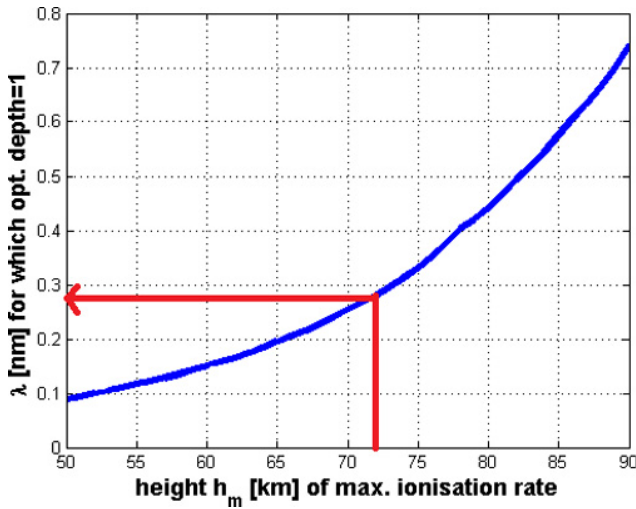


Fig. 1. Penetration depths of X-rays. At a height h_m , the optical depth of the wavelength denoted by the function is unity. The figure was generated based on wavelength vs. absorption cross section data from Nicolet and Aikin (1960) and Eq. (7). For example the red arrow points out that a h_m value of 72 km, which is consistent with our model calculations, is related to a center wavelength of 0.28 nm for the forcing X-rays.

VLF/LF propagation and it is convenient and useful to compare results with other authors using the effective height and steepness parameters h' and β , e.g. Cummer et al. (1998), McRae and Thomson (2000), Han and Cummer (2010), Han and Cummer (2011), Thomson et al. (2011a), Thomson et al. (2011b). Han and Cummer (2010) model midlatitude daytime D region ionosphere variations also with regard to flares in the two-parameter e-density profile framework.

The paper is organized as follows: at first we present the e-density model and its development in time during quiet and flare disturbed situations, then we discuss equilibrium solutions and their relation to other work. After a short description of the receiver and signal processing the propagation calculations using the LWPC (Long Wave Propagation Capability Code, Ferguson, 1989) are presented which we also use to discuss phase vs. height decrease and phase vs. X-flux relations. We end with drawing some conclusions.

2 Modeling electron density profiles

Wait and Spies (1964) proposed a well-known two-parameter electron density profile for the lower ionosphere (about 60–85 km height) which we use in the form (e.g. Cummer et al., 1998; Rodger et al., 2007; Han and Cummer, 2010):

$$n_e = n_0 e^{-0.15h'} e^{(\beta-0.15)(h-h')} = n_0 e^{-h/H} e^{\beta(h-h')}, \quad (1)$$

where $n_0 = 1.43 \times 10^{13} \text{ m}^{-3}$, scale height $H = 1/0.15 = 6.67 \text{ km}$ (corresponding to an isothermal atmosphere with

$T = 230 \text{ K}$) and the parameters h' (effective height, km) and β (profile steepness, $1/\text{km}$).

At $h = h'$ (this also holds for the following derivations):

$$n_e = n_0 e^{-h'/H}. \quad (2)$$

During flare forcing the electron density increases:

$$n_e = n_u + n_f, \quad (3)$$

where the undisturbed day value $n_u = n_0 e^{-h'_d/H}$. h'_d is the undisturbed (not flare affected) daylight effective height parameter. To get a good agreement between our propagation calculations and recorded amplitudes and phases, $h'_d = 71 \text{ km}$ for the NRK path and $h'_d = 73 \text{ km}$ for the GBZ path (quiet conditions) have been applied. Thomson et al. (2011a) and Thomson et al. (2011b) report h' values in the range 70–72 km.

For the time development of the e-density profile we use with (Rodger et al., 1998, 2007)

$$\frac{\partial n_e}{\partial t} = q_f(t - \tau_0) + q_u - \beta_i(h'(t))n_e - \alpha n_e^2, \quad (4)$$

where q_u and q_f are the ion-pairs produced per second in the undisturbed (not flare affected) case and by flares, respectively; α and β_i are the recombination and attachment coefficients, see below. A response delay of the order of $\tau_0 = 2 \text{ min}$ turned out to be appropriate during the propagation calculations.

For n_u we assume equilibrium (i.e. $\frac{\partial n_u}{\partial t} = 0$), yielding:

$$q_u = \beta_i n_u + \alpha n_u^2, \quad (5)$$

where n_u is also the initial condition for $n_e(t)$. For the propagation calculation Eq. (4) is numerically integrated using the classical Runge–Kutta algorithm.

For the ion pair production by X-rays in the lowest part of the ionosphere only a small wavelength range around $\lambda = 0.2\text{--}0.3 \text{ nm}$ is effective, longer wavelengths (lower energies) being absorbed at higher altitudes (cp. Fig. 1, see below).

We therefore use a Chapman function approach for q_f :

$$q_f(t) = p_0 X_{\text{sh}}(t) e^{1 - \frac{h'(t) - h_m}{H} - \frac{1}{\cos(z(t) - 90/94)}} e^{-\frac{h'(t) - h_m}{H}}. \quad (6)$$

At $h' = h_m$ this function (with $z = 0$) assumes its maximum and the optical depth τ of the vertically incident radiation is unity at this height (Budden, 1961):

$$\tau = \sigma n_n(h_m) H = 1. \quad (7)$$

Inserting $n_n(h_m) = n_{n0} e^{-h_m/H}$, which is the particle density of neutral air ($n_{n0} = 2.687 \times 10^{25} \text{ molecules per m}^3$ at sea level), with given h_m we can solve for σ , the absorption cross section of air. σ is highly λ dependent (see Nicolet and Aikin, 1960, Table 1 and Fig. 1, generated by us using their table values and Eq. 7). So from h_m – which we fit to

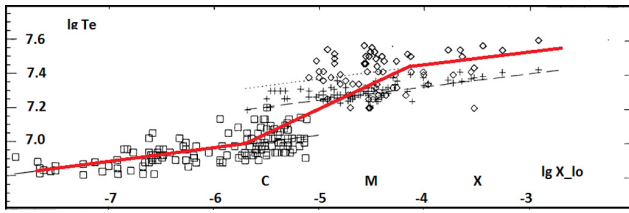


Fig. 2. Flare electron temperature vs. X-ray intensity (0.1–0.8 nm); adapted from Yuda et al. (1997), squares: S XV, crosses: Fe XXV, diamonds: Fe XXVI; red line: our fit.

our propagation data – we can infer the relevant X-ray wavelength for D-layer forcing in the height range in question.

X_{sh} is the X-ray flux in the range 0.05–0.4 nm wavelengths (24.8 down to 3.1 KeV) reaching the top of earth’s atmosphere. Together with the X-ray flux in the range 0.1–0.8 nm wavelengths (12.4 down to 1.55 KeV), called X_{I0} subsequently, these 2 bands are continuously monitored by the GOES XRS sensors (Geostationary Operations Environmental Satellite, www.swpc.noaa.gov/Data/goes.html, time resolution 1 min). The GOES data together with our own recorded VLF/LF amplitude and phase data are the inputs to our model.

With an average ionization energy of 35 eV for air molecules, we have $\frac{\text{ion-pairs}}{\text{Joule}} = \frac{1}{35\text{eV}} = 1.78 \times 10^{17} \text{ J}^{-1}$:

$$p_0 = 1.78 \times 10^{17} \frac{1}{eH} [\text{Jm}]^{-1} \quad (8)$$

cp. Budden (1961), $e = \exp(1)$. For arbitrary zenith angle z the function q_f (Eq. 6) assumes its maximum value $q_{f,\text{max}} = p_0 X_{sh} \cos(z \frac{90}{94})$ for $(h' - h_m)/H = -\ln(\cos(z \frac{90}{94}))$.

With Eq. (2) we have

$$h'(t) = -H \ln\left(\frac{n_e(t)}{n_0}\right). \quad (9)$$

With regard to β a saturation behavior is reported (Thomson et al., 2005; Grubor et al., 2008, cp. Fig. 4), which we model by

$$\beta(t) = \beta_d + (\beta_{\text{max}} - \beta_d) \left(1 - \frac{n_u}{n_e(t)}\right), \quad (10)$$

where β_d is the undisturbed profile steepness and $\beta_{\text{max}} = 0.55 \text{ km}^{-1}$. n_u is the undisturbed e-density at the undisturbed effective height $h'_d = -H \ln(\frac{n_u}{n_0})$. Inserting this in Eq. (10) yields an increasing β in terms of a height decrease $dh'(t) = h'_d - h'(t) \geq 0$:

$$\beta(t) = \beta_d + (\beta_{\text{max}} - \beta_d) \left(1 - e^{-\frac{dh'}{H}}\right). \quad (11)$$

For the recombination coefficient α below 84 km we set with Rodger et al. (2007):

$$\alpha = 5.0 \times 10^{-13} \left(\frac{T_i}{300}\right)^{-0.55} \text{ m}^2 \text{ s}^{-1}. \quad (12)$$

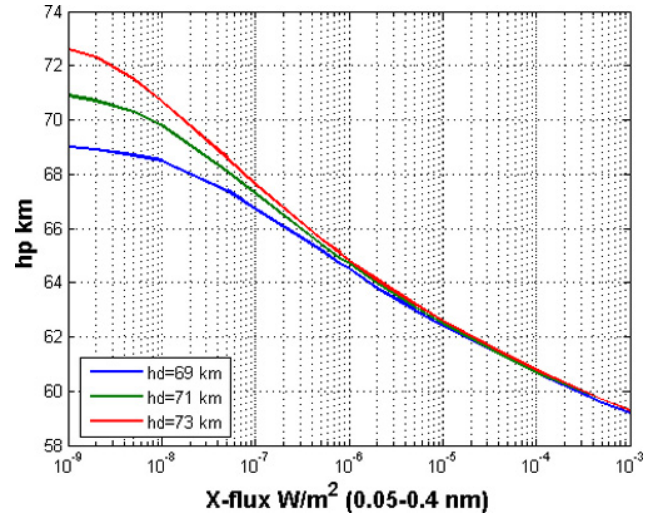


Fig. 3. height decrease vs. X-flux (0.05–0.4 nm). Sun zenith angle $z = 0$.

The attachment coefficient β_i during daytime is chosen according to Rodger et al. (1998). Because of its dependence on the product of the O_2 and N_2 densities for the process: $O_2 + e + N_2 \rightarrow O_2^- + N_2$ and the O_2 density squared for the process: $O_2 + e + O_2 \rightarrow O_2^- + O_2$, it strongly increases with decreasing height – from $\beta_i = 0.0004 \text{ s}^{-1}$ at 70 km to 0.02 s^{-1} at 60 km. Recombination and attachment coefficients also depend weakly on the ion temperature, which we choose as $T_i = 260 \text{ K}$ for a cold plasma. If we would neglect recombination, the inverse of β_i can be interpreted as the relaxation time of the e-density dynamics which decreases from about 38 min at 70 km height to 1 min at 60 km.

3 Equilibrium assessments

Before solving the time dependent equations we want to discuss the h' vs. X-flux relation assuming stationary conditions:

$$q_f(h') + q_u - \beta_i(h')n_e(h') - \alpha n_e^2(h') = 0. \quad (13)$$

This implicit equation can be solved numerically for h' . Figure 3 shows the resulting relation between h' and the X_{sh} -flux. For fluxes $> 10^{-7}$ we have $\Delta h' \approx 3 \text{ km}$ per X_{sh} -flux decade slowly diminishing with higher fluxes. For comparison from Fig. 8 in Han and Cummer (2010), the $\Delta h' = 3.5\text{--}5 \text{ km}$ per X_{sh} -flux decade can be read.

To compare our calculated h' vs. X_{sh} relation and results of different authors (Thomson et al., 2005; Grubor et al., 2008), we have to map X_{sh} to X_{I0} , because these results are mostly listed with respect to the lower energy (longer wavelength, 0.1–0.8 nm) band which is also used for the usual B, C, M, X flare classification.

For this purpose we assume the flare spectrum to be purely thermal bremsstrahlung dominated and get with respect to

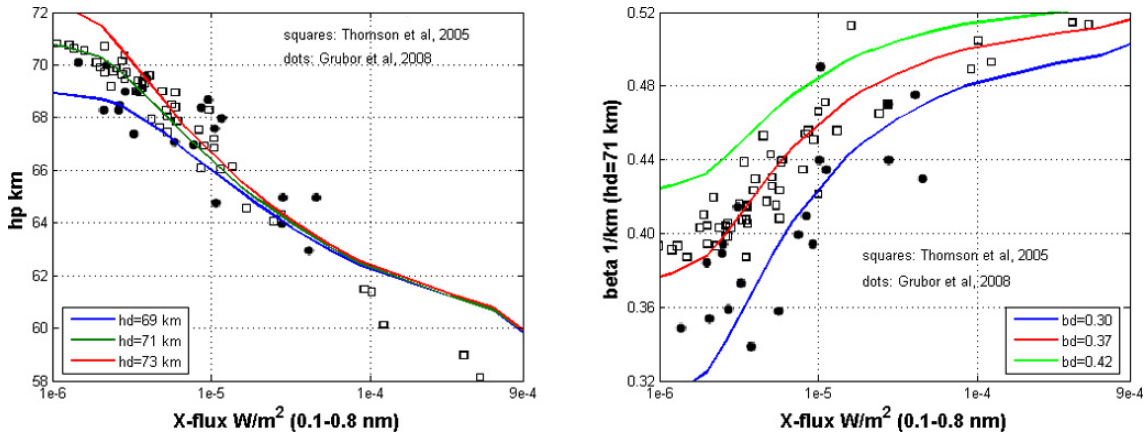


Fig. 4. Electron density profile height h' and steepness β vs. flare X-flux (0.1–0.8 nm) at sun zenith angle $z = 0$.

band center photon energies E_{sh} and E_{lo} for the photon flux ratio:

$$\frac{X_{lo}}{X_{sh}} = e^{-(E_{lo}-E_{sh})/(kT_e)} \tag{14}$$

Yuda et al. (1997) report a slight increase of the average electron (plasma) temperature T_e with total flare intensity. Based on the X_{lo} -band this can be parametrized by

$$T_e(X_{lo}) = A \cdot X_{lo}^n \tag{15}$$

Yuda et al. (1997) (see Fig. 5 therein) provide data of about 320 flares with regard to their maximum electron temperature gained from the intensity of sulfur and iron line radiation together with the X-flux X_{lo} . They present two fits for the flare ranges B1–M1 and M1–X10 with $n = 0.08$ and 2 different A-constants emphasizing the multi-thermal nature of weak and strong flares with rather weak intrinsic temperature-X-flux dependency.

Our own triple piecewise fit to these data yields (Fig. 2):
 $A = 3 \times 10^7$ and $n = 0.08$ for $X_{lo} \leq 2 \times 10^{-6} \text{ W m}^{-2}$,
 $A = 4.2 \times 10^8$ and $n = 0.28$ for $X_{lo} > 2 \times 10^{-6} \text{ W m}^{-2}$ and $X_{lo} \leq 1 \times 10^{-4} \text{ W m}^{-2}$,
 $A = 6.6 \times 10^7$ and $n = 0.08$ for $X_{lo} > 1 \times 10^{-4} \text{ W m}^{-2}$.

For example we have plasma temperatures of $T_e = 10, 18, 32$ megaK with C1, M1, X1 flares, respectively.

Now from Eqs. (14) and (15) with the constants just defined a function $X_{lo}(X_{sh})$ can be gained.

Figure 4 (left) shows the same relation as Fig. 3 but now displayed with respect to X_{lo} together with recorded data from 2 sources: Thomson et al. (2005), Grubor et al. (2008) for 3 different start values h'_d (undisturbed, day). The the β -X relation (right) is derived using Eq. (11) for 3 different start values β_d (undisturbed, day) together with recorded examples from Thomson et al. (2005) and Grubor et al. (2008).

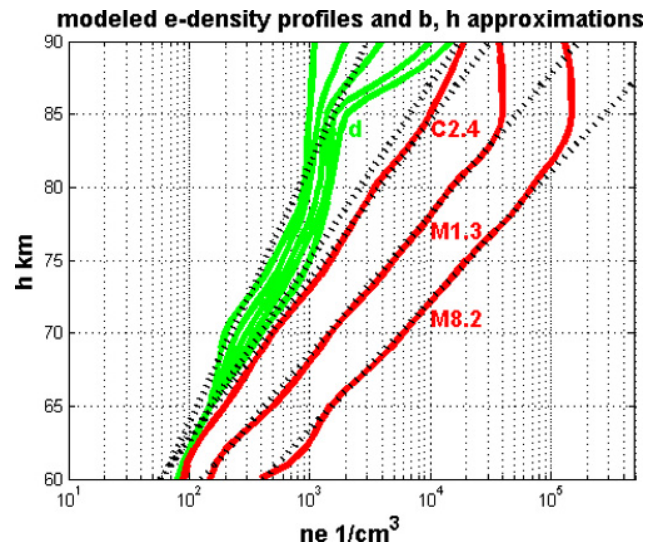


Fig. 5. Modeled e-density profiles from Nicolet and Aikin (1960): green: quiet day with zenith distances 70, 60, 50, 30, 0 degrees (from left to right); red: weak to strong flare conditions; dotted lines: equilibrium h' (km); β (km^{-1}) profiles from our model with the following values: quiet day: $h' = 72, \beta = 0.28, h' = 70, \beta = 0.34$, flares: h', β according to Fig. 4, center lines.

4 Reception and signal processing

Before comparing propagation calculations to our monitored signals, we give some information about the hard and software used. The receivers (one for each transmitter) have been set up by us with ferrite coils oriented for the maximum signal amplitude (horizontal magnetic field reception). After pre-amplification a stereo sound card computer interface with 192 kbit sample rate is used. The second channel is fed with the 1 s pulse of a GPS receiver. Our software reads each second a 170 ms signal train and extracts amplitude and phase with regard to the rising GPS-pulse flank. For a phase resolution of two degrees at a transmitter frequency

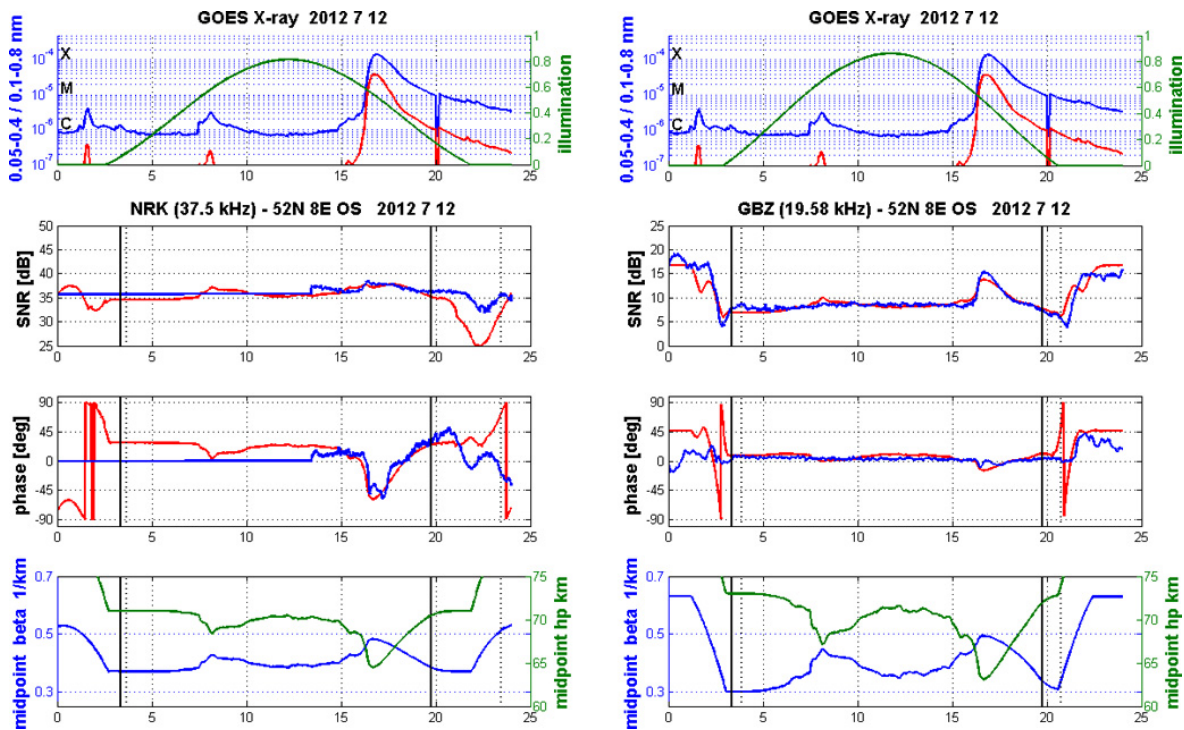


Fig. 6. On 12 July 2012 with X1.4 flare from sunspot group AR 1520 directly facing earth and peaking at 16:53 UT; left panel: NRK 37.5 kHz, $h_m = 74$ km, $h'_d = 71$ km, $\beta_d = 0.37$ km⁻¹, NRK recording starts at 13:30 UT; right panel: GBZ 19.58 kHz, $h_m = 71$ km, $h'_d = 73$ km, $\beta_d = 0.30$ km⁻¹. In the middle panels (amplitude and phase) blue and red are the recorded and calculated values, respectively. In the upper panels (here and in the following figures) the green function displays the cosine of suns zenith angle shifted to 94 degrees as start value with regard to an illumination height of about 70 km above ground.

of 37 kHz the GPS pulse flank detection has to be better than 150 ns. Both MSK transmitters are also GPS locked. This is not for all VLF/LF transmitters necessarily the case. For the amplitude the signal-to-noise ratio (SNR) is given. SNR = 0 dB is defined by the averaged signal level received during transmitter maintenance drop outs.

5 Propagation calculations and modeling results

For the propagation calculations the following parameters have been used (receiver at 52° N, 8° E):

NRK (37.5 kHz, $d = 2210$ km, bearing NW)

$h'_n = 84$ $\beta_n = 0.63$ $h'_d = 71$ $\beta_d = 0.37$ $h_m = 74$

GBZ (19.58 kHz, $d = 800$ km, bearing NW)

$h'_n = 84$ $\beta_n = 0.63$ $h'_d = 73$ $\beta_d = 0.30$ $h_m = 71-72$,

where h'_n , β_n , h'_d , β_d are the undisturbed h' (km) and β (km⁻¹) values for the night and day profiles. They are consistent with other work (e.g. Ferguson, 1989; Thomson et al., 2011a,b). The precise values as presented yield the electron density profiles with best fit of the propagation calculations with regard to the recorded data. The actual undisturbed $h'(t)$ and $\beta(t)$ values are linearly interpolated between the night and day values. From $h_m = 71-74$ km the effective absorption cross section of air can be calculated (Eq. 7) and the X-

ray wavelength belonging to that cross section can be looked up as 0.27–0.31 nm as the center wavelength for forcing the D layer (cp. Sect. 2 and Fig. 1).

Some modeling results are shown in Fig. 6 ff. LWPC propagation calculations together with the time integration of the electron density profile have been done in 1 min intervals and in 100 km distance slices along the propagation paths. Figures 6 and 7 display complete runs for the 2 days, 12 July 2012 and 18 August 2012 for NRK (left panels) and GBZ (right panels). The top panel shows the X-ray fluxes X_{10} and X_{sh} and, additionally, the $\cos(\text{zenith angle})$ function at midpath. The panels below show recorded (blue) and LWPC calculated amplitudes and phases (red) at the receiver site 52° N, 8° E. The bottom panels show the time course of the Wait and Spies parameters β and h' at midpath. The propagation calculations generate all these data in 100 km distance steps. Figure 8 presents an enlarged part of Fig. 7. The figure captions contain the chosen model parameters. In the following we discuss some results derived from these calculations fitted to our data.

5.1 Phase shift and height decrease

Wait (1959) derived an expression to assess the lower ionosphere height decrease Δh from phase shift measurements

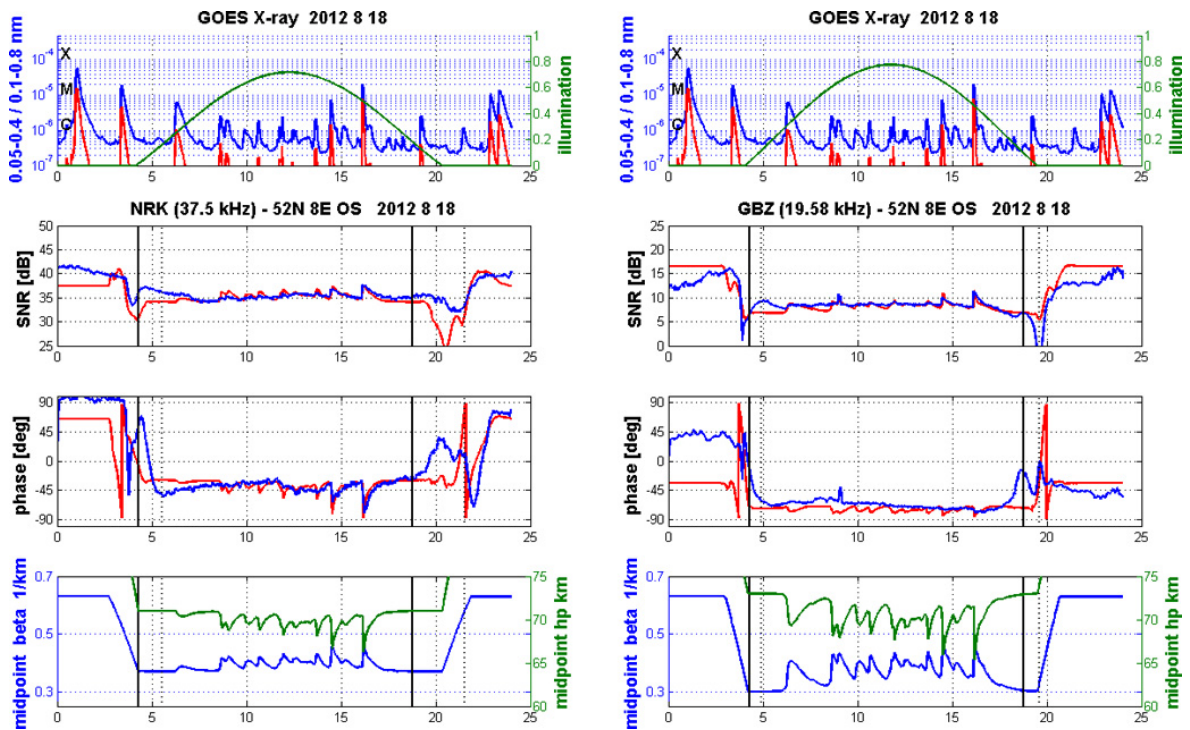


Fig. 7. On 18 August 2012; variety of C and M flares from sunspot group AR1542 near-solar limb; left panel: NRK 37.5 kHz, $h_m = 74$ km, $h'_d = 71$ km, $\beta_d = 0.37$ km⁻¹; right panel: GBZ 19.58 kHz, $h_m = 72$ km, $h'_d = 73$ km, $\beta_d = 0.30$ km⁻¹. In the middle panels (amplitude and phase) blue and red are the recorded and calculated values, respectively.

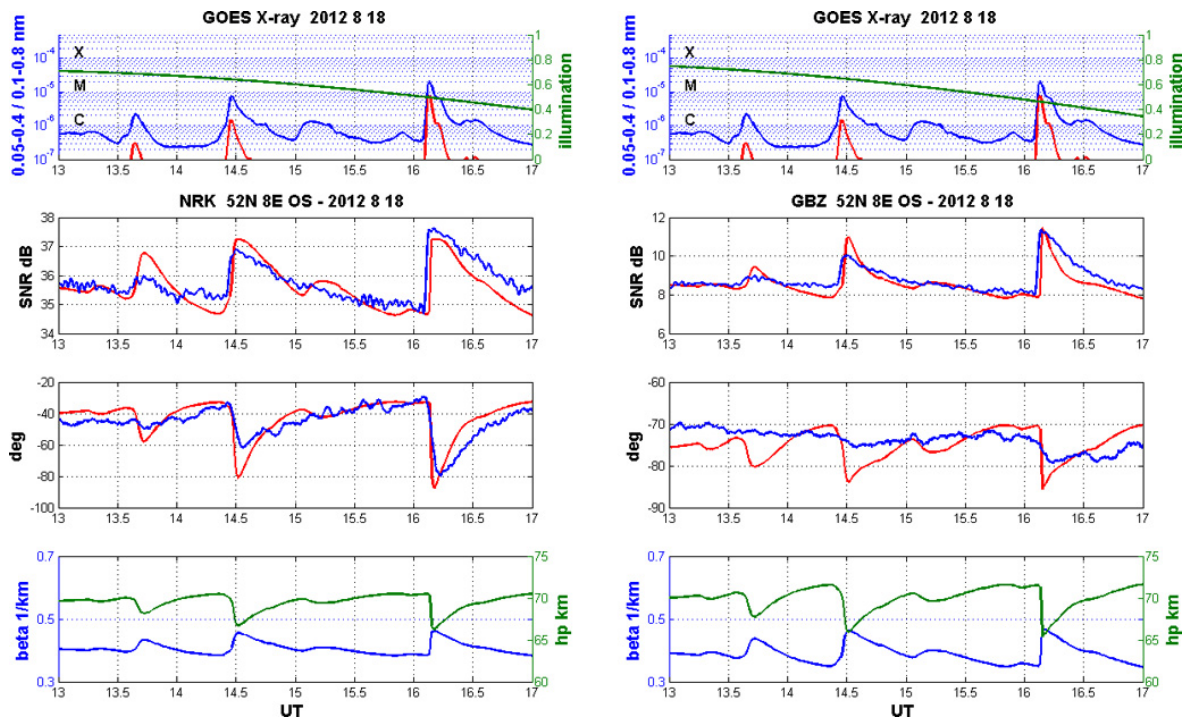


Fig. 8. On 18 August 2012, detail 13:00–17:00 UT; for the parameters see Fig. 7. In the middle panels (amplitude and phase) blue and red are the recorded and calculated values, respectively.

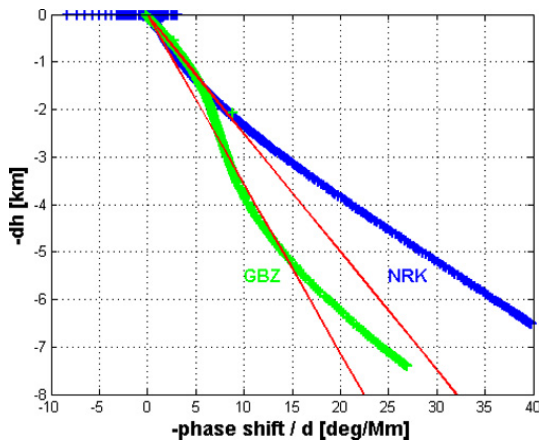


Fig. 9. Height decrease vs. phase shift per Mm. See Sect. 5.1.

and several authors made use of it, e.g. Kamada (1985), Khan et al. (2005). For a waveguide in 1st mode approximation, for small λ/h and small Δh he found a relation for the relative phase velocity decrease with decreasing reflection height from which, because of $\frac{\Delta v_p}{c} = \frac{\Delta \phi}{360} \frac{\lambda}{d}$, the phase shift per distance unit can be assessed (d : distance, a : earth radius):

$$\frac{\Delta \phi}{d} \simeq -\frac{360}{\lambda} \left(\frac{h}{2a} + \left(\frac{\lambda}{4h} \right)^2 \right) \frac{\Delta h}{h}. \quad (16)$$

Figure 9 shows this approximation (straight lines) together with results from our propagation calculations (12 July 2012, 18 August 2012, respectively). In both cases, especially NRK, increasing deviations with increasing Δh (large flare intensities) are obvious as expected and care should be taken in using the relation. Also for the short and medium sized distances in our examples (GBZ: 800, NRK: 2210 km) the first mode approximation is not valid yet, especially with GBZ.

5.2 Phase shift and X-flux

Figure 10 shows the relation between the LWPC-calculated phase delay per 1000 km (Mm) distance and X-flux (0.05–0.4 nm, left panel, 0.1–0.8 nm, right panel) for a C7 flare followed by a C1.5 flare on 18 August 2012 between 14.3 and 15.7 UT. We note that the flare enhanced X-flux in the short wavelength band extends 3 orders of magnitude and in the long wavelength band roughly 1.5 orders of magnitude. Displayed are examples for a hysteresis loop behavior of the phase delay during flares found by us with many other cases during our recordings and fitted model calculations: the phase decreases during the steep rise time of the flare, then decreases slowly around the peak time and recovers more slowly again during the flare tail relaxation time showing exponential decay in the case of the stronger flare (nearly linear phase vs. $\log(X\text{-flux})$). During the decay of the larger flare, the loop of a smaller one is superimposed. Hysteresis behavior of the effective height parameter decrease

during flares has been reported by Han and Cummer (2010). Due to the hysteresis behavior there is no functional relation between a phase value ϕ and a certain X-flux and. Such a functional relation however exists and is reported between the minimum phase delay and the peak X-flux for different flares. In the C7 case we read $\phi_{\min} = -22 \text{ degrees Mm}^{-1}$ (NRK) and $\phi_{\min} = -17 \text{ degrees Mm}^{-1}$ (GBZ) at a maximum flux of $X_{\text{lo,peak}} = 4.5 \times 10^{-5} \text{ W m}^{-2}$ (note that the illumination at that time is only 0.65, reducing C7 to effective C4.4, cp. Figs. 7 and 8). Relations of the form $\phi_{\min}(t)/d = a \lg(X_{\text{peak}}) + b$ are reported by several authors, e.g. Kaufmann and Paes De Barros (1969), Raulin et al. (2009), Belenkiy et al. (2006). Hysteresis behavior usually points to a memory effect or relaxation behavior of the forced system that approximatively may be described by a first order system with relaxation time τ . Let ϕ_d be the phase shift per Mm, then with forcing by $f(t) = a \lg(X(t)) + b$ (with different a , b for X_{lo} and X_{sh}) we have a 1st order differential equation

$$\dot{\phi}_d(t) + \frac{1}{\tau} \phi_d(t) = f(t). \quad (17)$$

The solution in Fourier space is

$$\tilde{\phi}_d(\omega) = \frac{\tau}{\sqrt{1 + (\omega\tau)^2}} e^{i\gamma} \tilde{f}(\omega). \quad (18)$$

The propagation phase shift per Mm, ϕ_d , reacts to forcing with radian frequency $\omega = 2\pi/T$ with a delay angle of $\gamma = \arctan(-\omega\tau)$. The hysteresis ellipses fitted to the data in Fig. 10, left panel, are parametrized by

$$(\lg(X(t)); \phi_d(t)) := (\sin(\omega t) + c_1; \phi_{d,\min}/2 \cdot \sin(\omega t + \gamma) + c_2),$$

where $\omega = 2\pi/T$ and $T = 84 \text{ min}$ (for the total flare time range 14.3–15.7 UT). For NRK using $\phi_{d,\min} = -22 \text{ deg Mm}^{-1}$ and $\gamma = -60 \text{ deg}$ we get $\tau = 23 \text{ min}$, which in this approximation is the lower ionosphere relaxation time as a combined result of the recombination and attachment processes. For GBZ the result is $\tau = 13 \text{ min}$. These values fit in between the relaxation times of 38 min at 70 km height and 1 min at 60 km height mentioned at the end of Sect. 2. GBZ at about half the frequency of NRK senses a deeper layer and a shorter relaxation time is plausible.

6 Conclusions

Using appropriate electron density profile height and steepness parameters (h' , β) as well as a Chapman function for the X-ray forcing our model yields a consistent representation of the amplitude and phase variations of VLF/LF radio signals that can be used to identify lower ionosphere parameters in the flare disturbed case. The approach is consistent with using the short wavelength flux in the range (X_{sh} , 0.05–0.4 nm) of a typical X-ray flare spectrum as the main forcing band for the ionosphere bottom, a result which is in agreement with the findings of Han and Cummer (2010). Peak

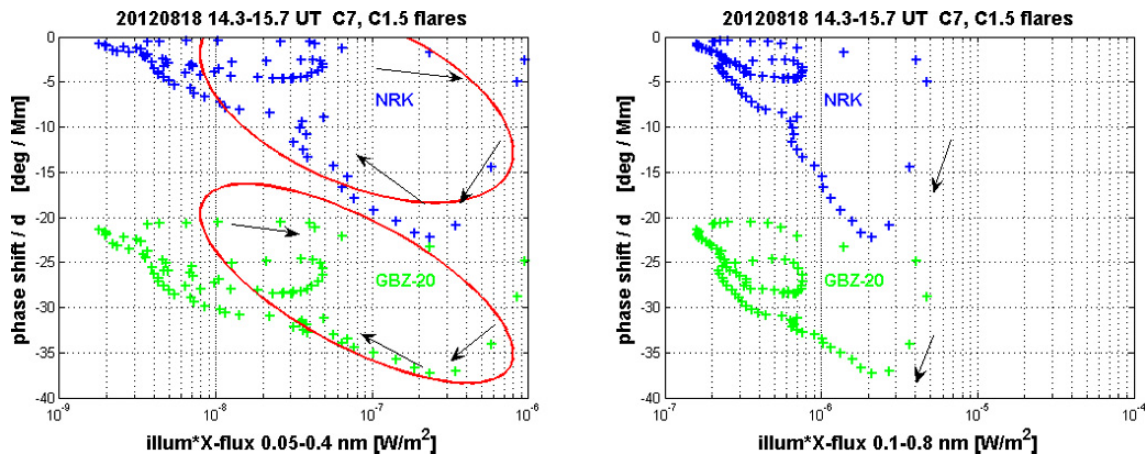


Fig. 10. Hysteresis loops of phase shift per Mm vs. $\cos(\text{zenith angle})$ corrected $\lg(\text{X-flux})$ (0.05–0.4 nm left panel, 0.1–0.8 nm, right panel) during 2 C-flares 20120818, cp. Figs. 7, 8. The arrows indicate the time development, the crosses are 1 min apart. The GBZ data are shifted by -20 degrees for better visibility. For the ellipses (left panel) see Sect. 5.2.

ionization heights h_m between 71 and 74 km are identified by our model calculations and point to a center wavelength between 0.27 and 0.30 nm (4.6–4.0 KeV). The dominant role of X_{sh} is plausible by noting that it is this part of the spectrum that penetrates down to the lowest part of the ionosphere which we remotely sense by VLF/LF radio waves. This is even more important with “hot” flares with enhanced line radiation at wavelengths of 0.185 nm and 0.155 nm (6.7 and 8 keV, respectively). Looking at equilibrium solutions allows for cross relations with earlier work regarding flare caused electron density profile height and steepness changes. Time integration yields some more detailed view on the electron density profile development during flares and its fingerprints on amplitude and phase delay of propagating signals. Some details of the relations between VLF/LF propagation phase shifts (SPAs, sudden phase anomalies), lower ionosphere effective height decrease and X-ray flux during solar flare caused sudden ionospheric disturbances (SIDs) have been highlighted. The hysteresis behavior of the phase delay vs. X-ray flux as a proxy for the flare forcing mechanisms will be one of the topics of further research.

Acknowledgements. Topical Editor C. Jacobi thanks S. Cummer and one anonymous referee for their help in evaluating this paper.

References

- Aiken, A. C.: The Ion Pair Production Function of the Lower Ionosphere, National Aeronautics and Space Administration. Goddard Space Flight Center, Technical report N70-18945, 1969.
- Aschwanden, M. J.: Solar Flare Physics Enlivened by TRACE and RHESSI, *J. Astrophys. Astr.*, 29, 115–124, 2008.
- Belenkiy, M. I., Orlov, A. B., Petrova, G. A., and Uvarov, A. N.: Modeling of the electron density profile of the lower ionosphere (45–75 km) for sudden ionospheric disturbance conditions based on the data on sudden phase anomalies of VLF signals, *Int. J. Geomagnetism and Aeronomy*, 6, GI3007, doi:10.1029/2005GI000113, 2006.
- Budden, K. G.: *Radio Waves in the Ionosphere*, Cambridge University Press, 1961.
- Cummer, S. A., Inan, U. S., and Bell, T. F.: Ionospheric D region remote sensing using VLF radio atmospherics, *Radio Sci.*, 33, 178–1792, 1998.
- Doschek, G. A.: The Electron Temperature and Fine Structure of Soft X-Ray Solar Flares, *The Astrophys. J.*, 527, 426–434, 1999.
- Ferguson, J. A.: *Computer Programs for Assessments of Long-Wavelength Radio Communications*, Version 2.0, Technical Document, SPAWAR Systems Center, San Diego, USA, May 1998.
- Grubor, D. P., Šulić, D. M., and Žigman, V.: Classification of X-ray solar flares regarding their effects on the lower ionosphere electron density profile, *Ann. Geophys.*, 26, 1731–1740, doi:10.5194/angeo-26-1731-2008, 2008.
- Han, F. and Cummer, S. A.: Midlatitude daytime D region ionosphere variability measured from radio atmospherics, *J. Geophys. Res.*, 115, A10314, doi:10.1029/2010JA015715, 2010.
- Han, F. and Cummer, S. A.: Daytime ionospheric D region sharpness derived from VLF radio atmospherics, *J. Geophys. Res.*, 116, A05314, doi:10.1029/2010JA016299, 2011.
- Kamada, T.: VLF sudden phase anomalies, *J. Geomag. Geoelectr.*, 37, 667–699, 1985.
- Kaufmann, P. and Paes De Barros, M. H.: Some relationships between solar X-ray bursts and SPA’s produced on VLF propagation in the lower ionosphere, *Solar Physics* 9, 478–486, 1969.
- Khan, I., Indira Devi, M., Arunamani, T., and Madhusudhana Rao, D. N.: A synoptic study of VLF sudden phase anomalies recorded at Visakhapatnam, *Earth Planets Space*, 57, 1073–1081, 2005.
- McRae, W. M. and Thomson, N. R.: VLF phase and amplitude: daytime ionospheric parameters, *J. Atmos. Solar-Terr. Phys.*, 62, 609–618, 2000.
- Nicolet, M. and Aikin, A. C.: The Formation of the D Region of the Ionosphere, *J. Geophys. Res.*, 65, 1469–1483, 1960.

- Phillips, K. J. H.: The Solar Flare 3.8–10 keV X-Ray Spectrum, *The Astrophys. Journal*, 605, 921–930, 2004.
- Raulin, R. P., Correia de Matos David, P., Hadano, R., Saraiva, A. C. V., Correia, E., and Kaufmann, P.: The south America VLF NETWORK (SAVNET) : Development, installation status, first results, *Geofisica Internacional*, 48, 255–263, 2009.
- Rodger, C. J., Molchanov, O. A., and Thomson, N. R.: Relaxation of transient ionization in the lower ionosphere, *J. Geophys. Res.*, 103, 6969–6975, 1998.
- Rodger, C. R., Clilverd, M. A., Thomson, N. R., Gamble, R. J., Sep-
paelae, A., Turunen, E., Meredith, N. P., Parrot, M., Sauvaud, J.
A., and Berthelier, J. J.: Radiation belt electron precipitation into
the atmosphere: Recovery from a geomagnetic storm, *J. Geo-
phys. Res.*, 112, A11307, doi:10.1029/2007JA012383, 2007.
- Schmitter, E. D.: Remote auroral activity detection and modeling
using low frequency transmitter signal reception at a midlati-
tude site, *Ann. Geophys.*, 28, 1807–1811, doi:10.5194/angeo-28-
1807-2010, 2010.
- Schmitter, E. D.: Data analysis of low frequency transmitter signals
received at a midlatitude site with regard to planetary wave activ-
ity, *Adv. Radio Sci.*, 10, 279–284, doi:10.5194/ars-10-279-2012,
2012.
- Thomson, N. R., Rodger, J. C., and Clilverd, A. M.: Large solar
flares and their ionospheric D-region enhancements, *J. Geophys.
Res.*, 110, A06306, doi:10.1029/2005JA011008, 2005.
- Thomson, N. R., Clilverd, M. A., and Rodger, C. J.: Daytime Mid-
Latitude D-region Parameters at Solar Minimum from Short Path
VLF Phase and Amplitude, *J. Geophys. Res.*, 116, A03310,
doi:10.1029/2010JA016248, 2011.
- Thomson, N. R., Rodger, C. J., and Clilverd, M. A.: Daytime D-
region Parameters from Long Path VLF Phase and Amplitude, *J.
Geophys. Res.*, 116, A11305, doi:10.1029/2011JA016910, 2011.
- Wait, J. R.: Diurnal Change of Ionospheric Heights Deduced from
Phase Velocity Measurements in VLF, *Proc. IRE*, 47, 998, May
1959.
- Wait, J. R. and Spies, K. P.: Characteristics of the Earth-ionosphere
waveguide for VLF radio waves, *NBS Tech. Note* 300, 1964.
- Yuda, S., Hiei, E., Takahashi, M., and Watanabe, T.: Electron Tem-
perature of Solar Flares Derived from Helium-Like Sulphur
Lines, *Publications of the Astronomical Society of Japan*, 49,
115–121, 1997.